

On the Parameters determining the Neutrino Flux from observed Active Galactic Nuclei

J. L. Bazo^a and A. M. Gago^b

Sección Física, Departamento de Ciencias,

Pontificia Universidad Católica del Perú, Apartado 1761, Lima, Perú

(Dated: November 2, 2018)

Abstract

Extrapolating from a sample of 39 AGNs, we examine the impact on the total number of high energy ν_μ induced events (PeV-EeV) expected in IceCube (a 1Km^3 “neutrino telescope”), due to variations in different parameters involved in the neutrino flux, such as the emission region geometry, the estimation models and distributions of the Doppler factor and the variability time. This work has been done taking into account different limits of the extragalactic neutrino flux.

Among our conclusions, we find, in the case of the largest variability time, that the cylindrical geometry hypothesis for the emission region, produce a separation of 3σ in the total number of events relative to the spherical hypothesis. In addition, for similar choices of the burst time, spherical geometry and for the upper neutrino flux bound, we obtain a separation of 2.5σ in the total number of events, for some of the Doppler factor estimations. These differences are undistinguishable for other input values.

PACS numbers: 95.85.Ry, 95.55.Vj, 98.62.Nx

Keywords: Neutrinos, AGN, IceCube, Doppler factor, Emission Region Geometry, Variability Time-scale, Spectrum.

^aElectronic address: jlbazo@fisica.pucp.edu.pe

^bElectronic address: agago@fisica.pucp.edu.pe

I. INTRODUCTION

Nowadays, there is a special interest in studying different cosmic rays sources, for instance, Active Galactic Nuclei (AGN) [1–3], Gamma Ray Bursts (GRB) [4–7], Dark Matter and others [8]. They all help us to understand the structure and formation of our Universe. In particular, AGNs are very attractive to investigate, given that they are one of the most powerful continuous sources of the highest energy particles in the universe.

Among these particles, AGNs produce copiously neutrinos. Due to their weak interaction with matter, neutrinos keep their flux unaltered in their travel from the AGN to Earth. This feature makes them an ideal tool for exploring physical processes within the AGNs.

At present, our knowledge about the parameters involved in the calculation of the extragalactic neutrino flux is not so accurate. In fact, there is not an absolute agreement about some aspects related to these parameters. This is the case of the model used to estimate the Doppler boosting factor (e.g. Equipartition [9, 10], Inverse Compton [9, 10] and Variability [11] models) and its distribution (power-law-like), the shape of the emission region [12] (e.g. spherical and cylindrical) and the variability time scale, which can vary from few minutes to many days. A good determination of the Doppler factor is a key ingredient to establish the intrinsic photon luminosity, directly related with the neutrino flux. In the same way, the shape of the emission region changes the volume considered in the particle density of target photons that interact with protons. In addition, the time of burst is inversely proportional to the neutrino flux, so that, if the variability time decreases, the neutrino flux increases.

It is straightforward to note that changes in these parameters affect directly the neutrino flux and, hence, imply modifications in the expected value of the total number of neutrinos that will be detected on Earth. Consequently, it would be interesting to know the range of variation of these events when different assumptions are made about the parameters. If the number of events changes in a noticeable way, these numbers can be used as a tool to test the model parameters.

In this paper, we study the impact of these variations in the total number of muon neutrino induced events that could be detected in IceCube [13]. This detector is one of the so called “neutrino telescopes” (e.g. Amanda, Antares, Nestor) and consists of arrays of photomultipliers, located in a Cherenkov medium (ice), under construction in the South Pole with a standard volume of 1Km^3 . We choose ten years of exposure in the energy range

of PeV-EeV. In spite of the fact, that this interval must contain a small number of events, it is convenient to be studied, considering the absence of background in this energy region. We model the neutrino flux based on a catalogue of 39 AGNs and extrapolate for a maximum flux given for different proposed limits, which are the Waxman-Bahcall [14], the benchmark used by the IceCube Collaboration [15] and the γ -ray bound [16].

II. AGNS AND THE UNIFIED MODEL

Active Galactic Nuclei are one of the brightest known objects in the Universe, with an observed luminosity ranging between $10^{42} - 10^{49}$ erg/s. According to the Unified Model of AGN [17], they have a central engine composed by an accretion disk orbiting a rotating super-massive black hole (10^6 to 10^{10} solar masses). The AGN is powered by an accretion rate of matter onto the super-massive hole of a few solar masses per year, possibly supplied by the rotational energy of the black hole.

The Unified Model also claims other characteristics of the AGNs, such as: two jets¹ moving in opposite directions and outwards to the accretion disk, an optically thick torus and radio lobes. Furthermore, for this model Seyferts, Quasars, Blazars and Radio Galaxies, are all AGN, only with different orientations as viewed from Earth, accretion rates and black hole masses. In this work, we assume this model including in our test sample all these types of galaxies.

III. NEUTRINO FLUX FROM AGN

We will consider as our working hypothesis [18] that within inner regions of AGN jets, protons are highly accelerated by sheet-like shock waves (blobs, knots or bursts) to energies up to the range of PeV-EeV, according to Fermi's stochastic acceleration. These protons should then interact with ambient photons emitted by the accretion disk from the thermal blackbody radiation (UV bump or blue bump, between 7×10^{14} Hz to 3×10^{15} Hz), leading to the $\Delta^+(1232)$ resonance and followed by the decays (pion from photo-production) $n\pi^+ \rightarrow \mu^+\nu_\mu \rightarrow \bar{\nu}_\mu e^+\nu_e$. Thus, through this cascade, a neutrino flux is produced.

¹ Generic AGN models do not necessarily involve jets.

In order to calculate the observed neutrino flux produced in each AGN, we begin with the following generic useful relation

$$\int_{E_{\nu}^{min}}^{E_{\nu}^{max}} E_{\nu} \frac{d\Phi_{\nu}}{dE_{\nu}} dE_{\nu} = \frac{L_{\nu}}{4\pi d_L^2}, \quad (1)$$

where the integration limits depend on the range of energies chosen to observe (in our case PeV-EeV), L_{ν} is the observed neutrino luminosity and d_L is the luminosity distance to the AGN, defined as

$$d_L = d_m(1 + z), \quad (2)$$

with z the redshift of the AGN and d_m the proper motion distance (see Eq. (B2) in App B).

The energy spectrum, $\frac{d\Phi_{\nu}}{dE_{\nu}}$, will be assumed to be proportional to

$$\frac{d\Phi_{\nu}}{dE_{\nu}} \propto E_{\nu}^{-p} \exp\left(-\frac{E_{\nu}}{E_{cut}^{AGN}}\right). \quad (3)$$

The typical power law energy dependence of the extragalactic neutrino flux is a resemblance of the proton spectrum, which is supposed to be accelerated by the Fermi's shock mechanism. The slope of the power law, p , is usually taken to be 2, the generic E_{ν}^{-2} . However, it can be considered in the range 1.3–2.7. The spectrum also includes an exponential cutoff depending on the AGNs maximum attainable energy, E_{cut}^{AGN} (we will assume a general cutoff of 10^{10} GeV).

Therefore, the exact neutrino spectrum formula is

$$\frac{d\Phi_{\nu}}{dE} = \frac{L_{\nu}}{4\pi d_L^2} \left(\int_{E_{\nu}^{min}}^{E_{\nu}^{max}} E_{\nu} E_{\nu}^{-p} \exp\left(-\frac{E_{\nu}}{E_{cut}^{AGN}}\right) dE_{\nu} \right)^{-1} E_{\nu}^{-p} \exp\left(-\frac{E_{\nu}}{E_{cut}^{AGN}}\right). \quad (4)$$

We focus our attention on the observable quantities that compose the neutrino luminosity. Then, to unfold this luminosity in terms of these observables, we start from the definition of luminosity

$$L_{\nu} = \frac{N_{\nu} \langle E_{\nu} \rangle}{\Delta t_{obs}}, \quad (5)$$

where N_{ν} is the number of produced neutrinos, $\langle E_{\nu} \rangle$ the mean neutrino energy and Δt_{obs} the observed variability time of the emission region. Now, we give N_{ν} from the neutrino production sequence explained at the beginning of the section

$$N_{\nu} = (br_{\Delta \rightarrow n\pi^+})(br_{\pi^+ \rightarrow \nu_{\mu}})N_{\Delta}, \quad (6)$$

where “ br ” stands for the branching ratio of the desired decay channel. This gives approximately $N_{\nu} \approx N_{\pi^+} \approx \frac{1}{2}N_{\Delta}$.

It is useful to express the neutrino energy in terms of the energy of the parent proton by

$$\langle E_\nu \rangle = \langle x_{p \rightarrow \pi^+} \rangle \langle x_{\pi \rightarrow \nu_\mu} \rangle \langle E_p \rangle , \quad (7)$$

where $\langle x \rangle$ represents the average fraction of energy transferred from the parent particle to the product, which numerically gives $E_\nu \approx \frac{1}{4}E_\mu \approx \frac{1}{4}(\frac{1}{5}E_p)$.

On the other hand, to find the number of produced Δ 's we use

$$N_\Delta = \Phi_p N_\gamma \sigma_{p\gamma \rightarrow \Delta} \Delta t_{obs} , \quad (8)$$

with Φ_p the initial flux of highly accelerated protons, N_γ the number of ambient photons from the UV bump and $\sigma_{p\pi \rightarrow \Delta} = 10^{-32} m^2$ the delta photo-production cross section. Φ_p and N_γ are given by

$$\Phi_p = \frac{L_p R}{\langle E_p \rangle V} , \quad N_\gamma = \frac{L_\gamma \Delta t_{obs}}{\langle E_\gamma \rangle} , \quad (9)$$

where L_p and L_γ are the proton and photon observed luminosities, respectively, $\langle E_\gamma \rangle$ is the mean photon energy (in the present work we take it to be 10 eV), R is the observed size² of the emission region and V the observed volume of the emission region. It must be noted that the size of the emission region and, consequently, its volume depend on four parameters: the Doppler factor (δ), the variability time scale (Δt_{obs}), the redshift (z) and the angle between the velocity vector of the knot and the line of sight (θ). The detailed description of R and the volume can be found in Sec. III A 2.

Replacing Eqs. (6 - 9) into Eq. (5), we obtain

$$L_\nu = \frac{(br_{\pi^+ \rightarrow \nu_\mu})(br_{\Delta \rightarrow n\pi^+}) \langle x_{p \rightarrow \pi^+} \rangle \langle x_{\pi \rightarrow \nu_\mu} \rangle L_p L_\gamma \Delta t_{obs} R \sigma_{p\gamma \rightarrow \Delta}}{\langle E_\gamma \rangle V} . \quad (10)$$

To write Eq. (10) in a more compact notation, we use the optical depth, τ , defined as

$$\tau = \frac{R}{\lambda_{p\gamma \rightarrow \Delta}} = R n_\gamma \sigma_{p\gamma \rightarrow \Delta} = R \frac{L_\gamma \Delta t_{obs}}{V \langle E_\gamma \rangle} \sigma_{p\gamma \rightarrow \Delta} , \quad (11)$$

where $\lambda_{p\gamma \rightarrow \Delta}$ is the proton interaction length, R , the observed size, which should be understood as the linear path traveled by the proton in the direction of movement through the ambient photons and we write K as

$$K = (br_{\pi^+ \rightarrow \nu_\mu})(br_{\Delta \rightarrow n\pi^+}) \langle x_{p \rightarrow \pi^+} \rangle \langle x_{\pi \rightarrow \nu_\mu} \rangle \approx 0.024 , \quad (12)$$

² In the case of a spherical or cylindrical emission region it corresponds to its radius.

where we have used $br_{\Delta \rightarrow \pi} = 0.5$, $br_{\pi \rightarrow \nu} = 0.9998$, $\langle x_{p \rightarrow \pi} \rangle = 0.2$ and $\langle x_{\pi \rightarrow \nu} \rangle = \frac{1}{4}$.

Since τ is a Lorentz invariant, we can go from the observer's frame to the frame attached to the knot, so that we can use a simple geometry (see Sec. III A 2) to describe the emission region, leaving τ as follows

$$\tau = \tau' = \frac{R'(\delta, \Delta t_{obs}, z, \theta)}{V'(\delta, \Delta t_{obs}, z, \theta)} \frac{L'_\gamma \Delta t'}{\langle E'_\gamma \rangle} \sigma_{p\gamma \rightarrow \Delta} = \frac{R'(\delta, \Delta t_{obs}, z, \theta)}{V'(\delta, \Delta t_{obs}, z, \theta)} \frac{L_\gamma \Delta t_{obs}}{\langle E_\gamma \rangle} \sigma_{p\gamma \rightarrow \Delta} . \quad (13)$$

where primed quantities refer to a quantity measured in the jet and recalling that $\frac{L_\gamma \Delta t_{obs}}{\langle E_\gamma \rangle}$ is itself a Lorentz invariant. This now gives for Eq. (10)

$$L_\nu = K \tau L_p . \quad (14)$$

However, not all L_p will be observed because part of it would have already interacted with the ambient photons to produce the Δ 's. Therefore, the intrinsic luminosity will be e^τ times the observed luminosity, $L_p = e^\tau L_{p_{obs}}$. In our analysis we take $L_{p_{obs}}$, which is still unknown, as 10% of the photon total luminosity [18]. In addition, we must take into account the possible absorption of π^+ into the source when the medium is optically thick and therefore will not give time for the π^+ to decay into neutrinos. In this case, we use the substitution suggested by Ref. [18], changing τ by $(1 - e^{-\tau})$. Thus, the factor $(1 - e^{-\tau})e^{(1-e^{-\tau})}$ accounts for the absorption of p and π^+ in the source. Finally the ν_μ and $\bar{\nu}_\mu$ differential flux emitted by an individual AGN source can be obtained, using Eq. (4), with

$$\begin{aligned} \frac{d\Phi_{\nu_\mu + \bar{\nu}_\mu}}{dE_\nu} &= \frac{2 \frac{0.1 K L_{\gamma_{obs}} [(1 - e^{-\tau}) e^{(1 - e^{-\tau})}]}{4\pi d_L^2}}{\int_{E_\nu^{min}}^{E_\nu^{max}} E_\nu E_\nu^{-p} \exp\left(-\frac{E_\nu}{E_{cut}^{AGN}}\right) dE_\nu} E_\nu^{-p} \exp\left(-\frac{E_\nu}{E_{cut}^{AGN}}\right) \\ &= F(\delta, V, \Delta t_{obs}, z, L_{\gamma_{obs}}, \theta, E_\nu^{max}, E_\nu^{min}) E_\nu^{-p} \exp\left(-\frac{E_\nu}{E_{cut}^{AGN}}\right) , \end{aligned} \quad (15)$$

where the factor 2 takes into account the contributions of ν_μ and $\bar{\nu}_\mu$ ³. The function F includes the parameters that we are going to study δ , V and Δt_{obs} (the calculation of θ is indirectly affected by the estimation model of δ).

³ The muon antineutrino produced after the μ^+ decay has almost the same average fraction of energy transferred from the π^+ , $\langle x_{\pi \rightarrow \nu_\mu} \rangle \approx \langle x_{\pi \rightarrow \bar{\nu}_\mu} \rangle$, because each lepton shares approximately equal energy.

A. Flux parameters to be analyzed

In this subsection we describe the different hypothesis in the neutrino flux parameters studied in this paper.

1. Doppler boosting factor

As we have shown in the section before, the Doppler factor, δ , is a piece in the flux formula. At present, there are various models for computing δ , which, in some cases, give different output values of δ for the same object. This disagreement could also imply differences in the flux that would be interesting to examine. For our work, we consider the following estimation models of δ :

- Equipartition δ (EQ) [9, 10]: This is calculated assuming the equipartition of energy between radiating particles and magnetic field and is obtained from the ratio of the observed and the maximum intrinsic brightness temperatures. The maximum intrinsic temperature is supposed to be the equipartition temperature.
- Inverse Compton δ (IC) [9, 10]: In this case, the Doppler factor is determined from the comparison of the observed and predicted X-ray fluxes, assuming that this is caused by inverse Compton scattering of synchrotron photons off the radiating particles.
- Variability δ (Var) [11]: This is obtained in a similar way to δ_{EQ} , but is weaker than this, since it takes the third root of temperatures' ratio. Additionally, it replaces the observed brightness temperature instead of the variability brightness temperature, which is estimated from a total flux density flares associated with VLBI components emerging from the AGN core, covering nearly 20 years of variations.
- Minimum δ (Min) [19]: This model is computed only from the proper motion data using the minimum δ value allowed by

$$\delta_{min} = \Gamma_{min} = \sqrt{1 + \beta_{app}^2} , \quad (16)$$

where Γ is the Lorentz factor and β_{app} the apparent transverse velocity in units of c (the speed of light). We are going to use this model independent estimation as a reference.

Due to different proper motion observations of underlying shocks for a single jet, there should be a rather broad range of Doppler factors [20]. Then, it follows that a certain distribution in δ must be taken into account when computing the neutrino flux. According to Ref.[20] it is consistent with a steep power law distribution of intrinsic Doppler factors. In our calculation, we fit with a power law ($\delta^{-\gamma}$) the data obtained for each type of calculation of δ , as described in Appendix. B. In Sec. V we explain how the neutrino flux is averaged over the fitted distribution.

2. Emission Region Geometry

In the study of the emission region geometry, we consider two possibilities for its shape in the proper frame: a spherical and a cylindrical volume. These models are based on the observed variability time Δt_{obs} [12]. However, we should state that Δt_{obs} could give, at most, the estimation of only one of the dimension of this region and therefore the other two should be inferred somehow from this. In this sense, the formulas given here are actually not relativistic transformations (as in App. A), but rather estimations and should not be misunderstood.

To understand the next formulas, it is appropriate to define a quantity $D = \frac{\delta}{1+z}$ that includes both the Doppler factor (δ) and the cosmological effects given by the redshift (z). The geometries are described as follows:

- Spherical geometry: it has two options for the jet-frame source radius R' . The first option, that we call **SphereA**, uses the common formula

$$R' = Dc\Delta t_{obs} . \quad (17)$$

The second option, that we call by **SphereB**, uses a refined formula for R' , that consider the angle to the line of sight, θ , and the shock velocity, β_{shock} (used value $\beta_{shock}=0.5$). This expression is given by [12]

$$R' = \frac{Dc\Delta t_{obs}}{\frac{1}{\sqrt{2}} \text{Abs} \left[\frac{1}{\beta_{shock}} - \Gamma D(\cos(\theta) - \beta) \right] + \frac{D \sin(\theta)}{\Gamma}} . \quad (18)$$

- Cylindrical geometry: with radius R' and jet-frame length l . The region is rapidly energized by a plane shock traveling along the jet, such that photons are emitted immediately after shock passage from a thin disk-like region downstream of the shock. From here on, we assume $l = aR'$, with a variable (used value $a = 2$).

$$R' = \frac{Dc\Delta t_{obs}}{\frac{a\Gamma}{2} \text{Abs} \left[\frac{1}{\beta_{shock}} - \Gamma D(\cos(\theta) - \beta) \right] + D \sin(\theta)} . \quad (19)$$

3. Variability Time Scale

The observed fluctuations over the whole spectrum in the AGNs, or variability time scales of the bursts, are one of the main characteristics of Active Galaxies [21]. This variability suggested that the emitting regions were extremely compact, leading to the hypothesis that AGN were powered by massive black holes.

The time scale varies according to the class of AGN and waveband of the spectrum. The shortest fluctuation observed in an AGN is attributed to Mrk421 with a 15 minutes duration. However, there have been variability on time scales of months to years [21]. In the case of blazars, a rapid variability or flaring is common. Observed short time scales of a day or more in the X-ray band are characteristic to TeV blazars (e.g. Mrk421, Mrk501, PKS2155-304). They have even substructures with shorter time scales of $10^3 - 10^5$ sec [22]. On the other hand, many EGRET sources had time scales of several days [18] and the optical waveband flares are fairly slow.

After this considerations, we choose the variability time scales ranging from 15 minutes to 10 days.

IV. OUR AGN SAMPLE

Although there are more than 876 Blazars, 11777 Seyfert-1 and 48921 Quasi Stellar Objects catalogued by Verón-Cetty (2003)[23], only few of them contain the parameters important for our interests. After a thorough search of AGN catalogs, we have built our own AGN sample from some of them, so that gathering their data, we included relevant information to our investigation, such as the proper motion of jet components, luminosity and different Doppler factor estimations. From the combination of Ref.[20], the latest and widest AGN survey available on proper motion observations, with Ref.[24], which includes

luminosities, and Ref.[9, 11], containing Doppler factor estimations, we have selected only the objects that have information on all parameters, remaining a sample of 39 AGN. In order to get a proper motion distribution for the AGN's jets we add more data in the proper motion observations from earlier surveys [10, 19, 25–28].

We must note that these multiple observations are not from the same epochs, which might introduce some uncertainties. However, we think that it is good enough for our purposes.

A. Description of the sample

Our total sample of 39 AGN, is divided into three sub-classes: 10 BL Lacs (blazars) (see Table I), 27 Core-dominated Quasars (see Table II) and 2 Radio Galaxies (see Table III). Tables [I,II,III] show the observational data that describes the properties of each source (i.e. AGN model parameters). The data is presented as follows:

- Column(1) International Astronomical Unit source designation [Name B1950].
- Column(2) Alternative source Name.
- Column(3) Redshift.
- Column(4) Monochromatic luminosity at 15 GHz, from [24], completed with [29].
- Column(5) Component identifier of the knot.
- Column(6) Angular radial speed: proper motion.
- Column(7) Equipartition Doppler factor, from [9].
- Column(8) Inverse Compton Doppler factor, from [9].
- Column(9) Variability Doppler factor, from [11].
- Column(10) Reference for proper motion.

A comment is in order, in our calculations of the neutrino flux, we need to use the UV luminosity $L_{\gamma_{obs}}$ in Eq. (15) (see Sec. III). For that reason we extrapolate the luminosity given in this sample, which is in the radio component of the spectrum, to find the UV luminosity. This estimate has been done in the following way: from the luminosity fractions (for different parts of the electromagnetic spectrum) of the set of AGNs presented in Ref. [30], we compute the average luminosity fractions, such that the radio part represents 0.52% and the optical-UV region 26%. Then, with the relation $L_{UV} \approx 50L_{rad}$ we do the extrapolation.

B. Sample characteristics

To better understand the characteristics of the AGN sample, we present in this subsection several histograms and comparisons of its most relevant properties.

We display in Fig. 1 the angular distribution, in right ascension and declination, of our sample's 39 AGNs. Most of the sources are located in the northern hemisphere due to the abundance of observatories in that region. Nevertheless, this bias does not affect our purposes, since we are going to consider the neutrino flux as isotropic.

We show in Fig. 2 the extrapolated UV luminosity (in the observer's frame) distribution of our sample. It can be seen that Quasars have the highest luminosity, with a mean value of 7.23×10^{46} erg/sec, while Blazars and Radio-Galaxies have 4.82×10^{45} erg/sec and 4.50×10^{45} erg/sec, respectively. These observations are consistent with our expectations, since Quasars are thought to be the most luminous objects in the universe.

In Fig. 3 we present the extrapolated UV luminosity versus its intrinsic counterpart, which was obtained using Eq. (A3), for each Doppler factor estimation model. From that equation we expect that in the case of a δ slightly greater than one, the observed luminosity should be higher than the intrinsic luminosity. This situation is reflected in our sample, where the observed luminosities for each AGN is higher than their corresponding intrinsic values, which is represented by the points below the straight line. This indicates that most AGN jets in the sample are moving towards Earth and suffer the Doppler boosting. Only few AGN, in the case of the Equipartition and Inverse Compton estimation models, have the opposite behavior. This is because, for these models, some Doppler factor estimates are lower than one. On the contrary, for the Variability model all Doppler factor estimates are greater than one, meaning that their luminosities will suffer the so called Doppler boosting.

The apparent transverse velocity distribution for each knot in the sample is shown in Fig. 4. From this plot it is clear to note that Quasars have higher values of apparent transverse velocities than Blazars and Radio Galaxies, which is in agreement with Fig. 2, due to the relationship between Doppler factor, which depends on the apparent transverse velocity, and luminosity. We also notice here that some of the AGN jets are moving away from Earth, which match with our observations in Fig. 3.

The distribution of the mean angle to the line of sight, calculated using the method described in Appendix B, is given in Fig. 5 for different Doppler factor estimation models.

As we could have supposed from the previous plots, we see that the majority of the AGN jets are pointing almost directly towards us. This fact does not entirely reflect the assumptions of the Unified Model, which predicts, in average, greater angles for Quasars and Radio-Galaxies, than we have in our histograms. Meanwhile, Blazars are compatible with small angles, which is expected, since their jets are pointing almost directly to us. The mean θ values found for the whole sample are for $\theta_{EQ} \approx 5.1^\circ$, $\theta_{IC} \approx 9.4^\circ$, $\theta_{Var} \approx 7.6^\circ$, and $\theta_{min} \approx 13.4^\circ$.

In Fig. 6 we plot the distribution of the Doppler factor for each estimation model. We note that the Equipartition and Inverse Compton cases give lower δ values than the Variability case. Their mean values are $\langle \delta_{EQ} \rangle = 8.00$, $\langle \delta_{IC} \rangle = 7.65$ and $\langle \delta_{Var} \rangle = 9.61$ and they range between $\delta_{EQ} = [0.14, 29]$, $\delta_{IC} = [0.15, 27]$ and $\delta_{Var} = [0.98, 26.21]$. We found that these histograms can be fitted with the expected power law distribution. After applying the distribution discussed in Appendix B we obtain: $\langle \delta_{EQ} \rangle = 8.11$, $\langle \delta_{IC} \rangle = 6.54$, $\langle \delta_{Var} \rangle = 8.49$ and $\langle \delta_{min} \rangle = 7.04$. These new values correspond to a power law distribution with negative slope ($\delta^{-\gamma}$) with exponent $\gamma_{EQ} = 0.38$, $\gamma_{IC} = 0.51$, $\gamma_{Var} = 0.53$, and $\gamma_{min} = 0.55$.

Finally, we compare in Fig. 7, using two-dimensional plots, the different types of estimations for the Doppler factor, δ_{EQ} , δ_{IC} and δ_{Var} . We find that δ_{EQ} and δ_{IC} are strongly correlated, in contrast, δ_{Var} is uncorrelated with any of them.

V. ν_μ -INDUCED EVENT NUMBER CALCULATION

We calculate the number of AGN-neutrino induced events observed on Earth within the context of the proposed IceCube [13] detector. As we are interested in astrophysical point sources (i.e. AGNs), we use muon neutrinos because they can achieve the highest angular resolution (0.7°) due to the large muon track, which allows to reconstruct their direction [31]. Moreover, ν_μ -induced events have a higher effective volume [31] than other neutrino flavors. We restrict our search to the highest energy events in the PeV-TeV range, within IceCube's sensitivity [13], thus we avoid the background signals from atmospheric neutrinos. Then, the number of $\nu_\mu + \bar{\nu}_\mu$ induced muon events is calculated by [8]

$$N_\mu = T \int d\Omega \int_{10^{15} \text{ eV}}^{10^{18} \text{ eV}} dE_{\nu_\mu} \left\langle \frac{d\phi_{\nu_\mu}}{dE_{\nu_\mu}} (E_{\nu_\mu}) \right\rangle_{tot} A_{eff} (E_{\nu_\mu}) P_{surv} (E_{\nu_\mu}, \theta) P_{\nu_\mu \rightarrow \mu} (E_{\nu_\mu}, \theta, E_\mu^{thr}) , \quad (20)$$

where T is the exposure time (we use 10 years in our calculations) and A_{eff} is the effective area of the detector, taken from Ref. [15]. Since, for this energy range, IceCube is capable of observing both hemispheres, we integrate over the whole celestial sphere. Notice that in this expression, θ corresponds to the zenith angle ($\theta = 0$ is pointing to the South Pole) and should not be confused with the angle to the line of sight used to describe the neutrino flux in the previous sections.

The total isotropic flux of AGN neutrinos summed over all sources is defined as

$$\begin{aligned} \left\langle \frac{d\phi_{\nu_\mu}}{dE_{\nu_\mu}} \right\rangle_{tot} &= C_n \sum_{j=1}^{39} \left(\int_{\delta_{minj}}^{\delta_{maxj}} d\delta \, pdf(\delta)_{j,mod} F_j \left(\delta, V, \Delta t, z_j, L_{\gamma_{obsj}}, \langle \theta \rangle_{(j)mod}, 10^{18} \text{ eV}, 10^{15} \text{ eV} \right) \right) \\ &\quad \times E_\nu^{-p} \exp \left(-\frac{E_\nu}{E_{cut}^{AGN}} \right) \\ &= C_n \langle \phi \rangle_{tot} \times E_\nu^{-p} \exp \left(-\frac{E_\nu}{E_{cut}^{AGN}} \right), \end{aligned} \quad (21)$$

where $\langle \phi \rangle_{tot}$ represents the sum of the terms F_j (see Eq. (15)), after averaged over the probability density function (pdf) in δ , defined for each j source of the total 39 AGN sources of our sample. The probability density function varies for each estimation model (mod) and is given by

$$pdf(\delta)_{j,mod} = \frac{\delta^{-\gamma}}{\int_{\delta_{minj}}^{\delta_{maxj}} \delta^{-\gamma} d\delta}, \quad (22)$$

where γ corresponds to each Doppler factor estimation model ($\gamma_{EQ} = 0.49$, $\gamma_{IC} = 0.58$, $\gamma_{Var} = 0.55$, $\gamma_{min} = 0.76$). The integration limits, δ_{maxj} and δ_{minj} , are chosen for a single AGN source, taking the maximum (δ_{maxj}) and minimum (δ_{minj}) of its corresponding set⁴ of Doppler factors (these limits depend on the δ estimation model). The normalization constant C_n in Eq. (21) allows us to extrapolate the total ν_μ flux of our small sample to the maximum possible. This constant is given by

$$C_n = \frac{\phi_{bound}}{\langle \phi \rangle_{tot}^{max}}, \quad (23)$$

where ϕ_{bound} stands for the three different limits that we have chosen: the Waxman-Bahcall limit $3 \times 10^{-8} \text{ GeV}^{-1} \text{cm}^{-2} \text{s}^{-1} \text{sr}^{-1}$ [14], the benchmark used by the IceCube Collab. $1 \times 10^{-7} \text{ GeV}^{-1} \text{cm}^{-2} \text{s}^{-1} \text{sr}^{-1}$ [15] and the γ -ray bound $6 \times 10^{-7} \text{ GeV}^{-1} \text{cm}^{-2} \text{s}^{-1} \text{sr}^{-1}$ [16]. We must

⁴ When there is only one value for an AGN source, we assume an average range.

note that the given bounds are still below the limits set by recent experiments and above IceCube's sensitivity [15]. The limit for energies between 1 PeV and 3 EeV from the latest AMANDA results [32] derived with a 90% C.L. is $E^2\Phi_\nu(E) < 0.99 \times 10^{-6} \text{ GeV}^{-1}\text{cm}^{-2}\text{s}^{-1}\text{sr}^{-1}$ and the AMANDA-II-2000 data is still being processed. $\langle\phi\rangle_{tot}^{max}$ at 1 GeV, is the maximum value among the set of values of $\langle\phi\rangle_{tot}$ obtained for all the variations performed in our work (different types of δ estimation, class of geometry emission region and variability time of the burst). It is relevant to mention that there is a possibility that these sources were optically thick enough to absorb most of the protons, only allowing neutrinos to scape, which would indeed exceed the conservative WB bound.

Continuing with the description of Eq. (20) we define $P_{surv}(E_{\nu_\mu}, \theta)$, the survival probability of a neutrino crossing the Earth, by

$$P_{surv}(E_{\nu_\mu}, \theta) \equiv \exp \left[-\frac{\chi(\theta)}{L_{int}^{tot}(E_{\nu_\mu})} \right], \quad (24)$$

where $\chi(\theta)$ is the column density given by

$$\chi(\theta) \equiv \int_0^{l_{\nu_\mu}(\theta)} \rho(r(\theta, l)) dl, \quad (25)$$

with, l_{ν_μ} , the neutrino distance traveled through Earth calculated using

$$l_{\nu_\mu}(\theta) = \sqrt{(R_E - d)^2 \cos^2(\theta) + 2dR_E - d^2} - (R_E - d) \cos(\theta), \quad (26)$$

where R_E is the Earth's radius (6378 Km) and d the distance to the detector (for IceCube it is 1.4 Km).

In Eq. (25) we integrate over the neutrino path crossing the Earth using the parameterized Earth's density, $\rho(r)$, given by the Preliminary Earth Model (PREM [33]) and the inclusive interaction length, L_{int}^{tot} , is given by

$$L_{int}^{tot}(E_{\nu_\mu}) \equiv \frac{1}{\sigma_{\nu N}^{tot}(E_{\nu_\mu}) N_{Av}}, \quad (27)$$

where the inclusive cross section, $\sigma_{\nu N}^{tot}$, is taken from Ref. [34], which includes the charged and neutral current contributions.

The probability that a muon produced in a ν_μ charged current interaction reaches the detector before losing all its energy down to a value lower than the detector's energy threshold

E_μ^{thr} (10^3 GeV for IceCube) is defined by ⁵

$$P_{\nu_\mu \rightarrow \mu}(E_{\nu_\mu}, \theta, E_\mu^{thr}) \equiv \frac{1}{\sigma_{CC}(E_{\nu_\mu})} \int_0^{1 - \frac{E_\mu^{thr}}{E_{\nu_\mu}}} dy \frac{d\sigma_{cc}}{dy}(E_{\nu_\mu}, y) \left(1 - \exp \left[-\frac{R_\mu(E_{\nu_\mu}, \theta, E_\mu^{thr})}{L_{int}^{cc}(E_{\nu_\mu})} \right] \right), \quad (28)$$

where the differential charged current cross section, $\frac{d\sigma_{cc}}{dy}$ is taken from Ref. [35] and the muon range, R_μ , is taken from Ref. [36].

We include the effects of neutrino oscillations [37] by multiplying Eq. (20) by 0.5, given that the ratio of the initial to the oscillated muon neutrino flux, $\phi_{\nu_\mu} : \phi_{\nu_\mu}^{osc}$, would be 2:1.

It is worth mentioning that there are other scenarios where muons can lose a significant amount of energy before their decay, equivalent to considering only a single ν_μ [38], otherwise we would have to consider half of the neutrino flux (without neutrino oscillations), which is different from the one we assume here.

VI. RESULTS

We present in Fig. 8, Fig. 9 and Fig. 10, an analysis of the dependence of the expected total number of induced ν_μ and $\bar{\nu}_\mu$ events versus the variability time (ranging from 15 minutes to 10 days) for different Doppler factor estimation models, emission region geometries, and for ten years of exposure in IceCube. We use the generic spectrum E_ν^{-2} and normalize the figures with the WB limit (Fig. 8), the IceCube Collab. benchmark (Fig. 9) and the γ -ray bound (Fig. 10). In each figure we show four plots related to the different type of δ , where we display four curves corresponding to the following hypotheses in the geometry of the emission region: SphereB, Cylinder, SphereB-D and Cylinder-D (the last two are averaged over the δ distribution).

In general, we observe that the tendencies of the three figures are the same and they only differ in the scale of number of events. The behaviour in Δt_{obs} of the curves within each figure, can be understood from the factor $(1 - e^{-\tau})e^{(1-e^{-\tau})}$ in Eq. (15), with $\tau \propto 1/\Delta t_{obs}$. Also, using this factor, we can comprehend two important features of our plots. First, we see why all the graphs converge to the same number of events (given for the flux limit) for an small Δt_{obs} , which implies that for this time we are not able to distinguish among the

⁵ For down-going muons if $R_\mu(\theta) > d$, then we chose $R_\mu(\theta) = d$, because the Earth's density traversed by neutrinos is smaller.

different model parameters under study. Second, we observe the hierarchy of the curves, where the number of events is higher for the cylinder than for the sphere geometry. This is not strange since the spherical hypothesis gives a greater volume than the cylindrical one, which implies fewer number of events given that $\tau \propto 1/V$. Furthermore, comparing the number of events for the same geometry, we obtain slightly higher values in the case where we average over the Doppler factor distribution; this is because the distribution includes lower values of δ , which gives, in general, a greater number of events.

In order to quantify the differences observed in our plots, at the largest variability time, in the number of events, for the different parameter hypotheses studied (e.g. type of geometries and Doppler factor calculations), we have defined the following estimator:

$$N_\sigma = \frac{|N_{hyp(i)}^{limit} - N_{hyp(j)}^{limit}|}{\sqrt{N_{hyp(j)}^{limit}}}, \quad (29)$$

which gives us these discrepancies in terms of the number of σ 's, with $N_{hyp(i)}^{limit}$ the total number of expected neutrinos, where *limit* stands for the bound used in the extragalactic neutrino flux and $hyp_{(i)}$ refers to the various hypotheses compared.

Our first analysis has the purpose to evaluate how large the differences in the number of events are for the spherical and cylindrical geometry. This is shown in Table IV, where we have substituted in Eq. (29) $hyp_{(j)} = \text{SphereB}(\text{SphereB-D})$ and $hyp_{(i)} = \text{Cylinder}(\text{Cylinder-D})$, evaluated for each type of Doppler calculation. From this Table, we can see that, in the case of the WB limit, the differences go from 0.75σ to 1.53σ , when we do not include the δ distribution. Meanwhile, when the δ distribution is considered, these differences are even smaller going from 0.53σ to 0.89σ . For the IceCube benchmark, the differences are significant and range between $1.36\text{-}2.79\sigma$ and $1.02\text{-}1.62\sigma$ for the cases without and with δ distribution, respectively. For the γ -ray bound the differences are greater, ranging from $3.34\text{-}6.84\sigma$ and $2.35\text{-}3.98\sigma$ as described before.

In addition, we have done an analysis similar to the one before, only that in this case we have calculated the differences in the number of events considering the six different pairs of Doppler calculation's types. This is displayed in Table V and Table VI, for a specific geometry, spherical and cylindrical, respectively. There are only two favourable situations for discriminating the Doppler factor models using the number of events. This is for the case of a spherical geometry, the γ -ray bound and without δ distribution, where we have obtained

2.67σ in separation for the events predicted using δ_{EQ} and δ_{IC} . The other case is when we compare δ_{IC} and δ_{Var} , where we have got 3.05σ . For all the rest of pair comparisons we have got negligible differences, less than 1.6σ in the splitting of the number of events.

In spite of not including variations in “ a ”, the relation between the radius and the length in the cylinder ($l = ra$), we have checked that these changes will not lead to a relevant difference in the number of events.

As complementary information, we show in Fig. 11 the total number of expected events, for the three flux bounds, as a function of the slope p of the AGN spectrum, ranging from 1.3 to 2.7. It is clear that in $p = 2$ the number of events in this figure coincides with the maximum number of events in our precedent figures. Thus, from this plot we can rescale the results given in our tables, only multiplying the N_σ by $\sqrt{N_\mu(p)/N_\mu(p=2)}$, which at $p = 2.7$ is around $\sqrt{2}$.

VII. CONCLUSIONS

We have studied different neutrino production scenarios in AGNs for the highest energy neutrinos (PeV-Eev) and their impact in the total expected ν_μ -induced events in the IceCube detector, due to variations in the emission region geometry, the Doppler factor estimation model and the variability time. We have obtained the total neutrino flux based on a sample of 39 AGN (i.e. point sources observations), where the limits in the total neutrino flux were the WB bound, the IceCube Collab. benchmark and the γ -ray bound.

We have found as a global behaviour that if most AGN had long times of burst, which seems natural to assume, we should be able to distinguish, in some cases, among the different models. Otherwise, for small times of burst, no information about these model parameters could be extracted through neutrino observation in a detector with the capabilities of IceCube.

More specifically, for a 10-day fluctuation time and the γ -ray flux limit ($6 \times 10^{-7} \text{ GeV}^{-1}\text{cm}^{-2}\text{s}^{-1}\text{sr}^{-1}$), we could determine the emission region geometry after 10 years of IceCube exposure. We observe a separation greater than 3σ in the total number of events, between the cylindrical and spherical geometry, for all the δ cases. On the other hand, if the flux bound was below the WB limit ($3 \times 10^{-8} \text{ GeV}^{-1}\text{cm}^{-2}\text{s}^{-1}\text{sr}^{-1}$), the geometry would not introduce major changes in the total number of events. When the benchmark is 1×10^{-7}

$\text{GeV}^{-1}\text{cm}^{-2}\text{s}^{-1}\text{sr}^{-1}$, we are able to discriminate between geometries in half of the δ cases, without including the δ distribution, with a separation in the total number of events greater than 2σ .

It is important to note that it is possible to infer from Fig. 8, Fig. 9 and Fig. 10, any intermediate case (a mixture of both geometries), between the cylindrical and spherical geometry for the emission region. In this sense, how far or close we are from some of these extreme behaviours (purely cylindrical or spherical) is a measure of the tendency of the sample.

For the Doppler factor estimation models, in most cases, the total number of neutrino induced events gives no relevant information or, in other words, the differences in δ do not affect this number. Nonetheless, for a spherical emission region, $\Delta t_{obs} = 10$ days, the γ -ray bound and without considering the δ distribution, it is possible to distinguish between $\delta_{EQ}-\delta_{IC}$ and $\delta_{IC}-\delta_{Var}$ obtaining an event separation greater than 2.5σ .

It is relevant to keep on mind that our analysis has considered that the neutrino spectrum had slope $p = 2$. Therefore, for a slope $p > 2$, the separation in terms of N_σ must increase, which means that we are going to enlarge the number of cases where we can differentiate the geometries and the Doppler factor estimations models.

As closing remarks, we must say that our work establish possible tendencies in the parameters in the AGNs. In fact, we expect that these tendencies become more robust and measurable in the future, when we have a bigger sample containing the necessary information and accurate point sources observations.

Acknowledgments

This work was supported by Dirección Académica de Investigación (**DAI**), Pontificia Universidad Católica del Perú, 2004.

-
- [1] F. Halzen, E. Zas, *Astrophys.J.*, 488 (1997) 669 [arXiv:astro-ph/9702193]
 - [2] A. Atoyan and C. D. Dermer, *New Astron.Rev.*, 48 (2004) 381 [arXiv:astro-ph/0402646]
 - [3] J. K. Becker, P. L. Biermann, W. Rhode, to be published in *Astroparticle Physics* [arXiv:astro-ph/0502089]
 - [4] J. Alvarez-Muniz, F. Halzen, D. W. Hooper, *Phys.Rev.*, D **62** (2000) 093015 [arXiv:astro-ph/0006027]
 - [5] J. Alvarez-Muiz, F. Halzen, D. Hooper, *Astrophys.J.*, 604 (2004) L85 [arXiv:astro-ph/0310417]
 - [6] C. D. Dermer and A. Atoyan, *New Astron.Rev.*, 48 (2004) 453 [arXiv:astro-ph/0312591]
 - [7] D. Guetta, D. Hooper, J. Alvarez-Muniz, F. Halzen, E. Reuveni, *Astropart.Phys.*, 20 (2004) 429 [arXiv:astro-ph/0302524].
 - [8] J. Alvarez-Muniz, J. L. Feng, F. Halzen, T. Han, D. Hooper, *Phys.Rev.*, D**65** (2002) 124015 [arXiv:hep-ph/0202081].
 - [9] A. Güijosa and R. A. Daly, *ApJ*, 461 (1996) 600.
 - [10] E. J. Guerra and R. A. Daly, *ApJ*, 491 (1997) 483 [arXiv:astro-ph/9707124].
 - [11] A. Lähteenmäki and E. Valtaoja, *ApJ*, 521 (1999) 493.
 - [12] R. J. Protheroe, accepted by Publications of the Astronomical Society of Australia (PASA) (2002) [arXiv:astro-ph/0209111].
 - [13] The IceCube Collaboration, *IceCube Preliminary Design Document* (2001)
 - [14] E. Waxman and J. N. Bahcall, *Phys. Rev.*, D **59** (1999) 023002 [arXiv:hep-ph/9807282].
 - [15] IceCube Collab. *Astropart.Phys.*, 20 (2004) 507 [arXiv:astro-ph/0305196].
 - [16] O. E. Kalashev, V. A. Kuzmin, D. V. Semikoz, G. Sigl, *Phys.Rev.*, D**66** (2002) 063004 [arXiv:hep-ph/0205050].
 - [17] C. M. Urry and P. Padovani, *Publ.Astron.Soc.Pac.*, 107 (1995) 803 [arXiv:astro-ph/9506063].
 - [18] F. Halzen and D. Hooper, *Rept.Prog.Phys.*, 65 (2002) 1025 [arXiv:astro-ph/0204527].
 - [19] G. Guisellini, 1993 *ApJ*, 407 (1993) 65.
 - [20] K. I. Kellermann, *et al.*, *ApJ*, 609 (2004) 539 [arXiv:astro-ph/0403320].
 - [21] P. Uttley and I. M. McHardy, *Prog.Theor.Phys.Suppl.*, 155 (2004) 170 [arXiv:astro-ph/0402407].
 - [22] C. Tanihata et al., *Astrophys.J.*, 563 (2001) 569 [arXiv:astro-ph/0108310].

- [23] M. P. Véron-Cetty and P. Véron, *Astron. Astrophys.*, 412 (2003) 399
- [24] K. I. Kellermann *et al.*, *AJ*, 115 (1998) 1295
- [25] D. C. Homan *et al.*, *ApJ*, 549 (2001) 840 [arXiv:astro-ph/0009301].
- [26] S. G. Jorstad *et al.*, *ApJ*, 134 (2001) 181 [arXiv:astro-ph/0101570].
- [27] M. H. Cohen *et al.*, *ApJ*, 329 (1988) 1.
- [28] R. C. Vermeulen and M. H. Cohen, *ApJ*, 430 (1994) 467.
- [29] J. A. Zensus *et al.*, *AJ*, 124 (2002) 662
- [30] C. D. Impey and G. Neugebauer, *AJ*, 95 (1988) 307
- [31] IceCube Collab., A. Karle *et al.*, to be published with the proceedings of the XXth Inter. Conf. on Neutrino Physics and Astrophysics, Munich (2002) [arXiv:astro-ph/0209556].
- [32] K. Woschnagg, *et al.* (AMANDA Collab.) *Nucl. Phys., B* 143 (2005) 343 [arXiv:astro-ph/0409423].
- [33] A. M. Dziewonski and D. L. Andersson, *Physics of the Earth and Planetary Interiors*, 25 (1981) 297.
- [34] R. Gandhi *et al.*, *Phys. Rev. D*, **58** (1998) 093009 [arXiv:hep-ph/9807264] .
- [35] R. Gandhi, C. Quigg, M. H. Reno, I. Sarcevic, *Astropart.Phys.*, 5 (1996) 81 [arXiv:hep-ph/9512364].
- [36] P. Lipari and T. Stanev, *Phys. Rev.*, **D44** (1991) 3543.
- [37] J. F. Beacom *et al.*, *Phys. Rev.*, **D 68** (2003) 093005 [arXiv:hep-ph/0307025].
- [38] A. Levinson and E. Waxman, *Phys.Rev.Lett.*, 87 (2001) 171101 [arXiv:hep-ph/0106102].
- [39] S. M. Carroll and W. H. Press, *Annu. Rev. Astron. Astrophys.*, 30 (1992) 499.
- [40] C. L. Bennett *et al.*, *Astrophys.J.Suppl.*, 148 (2003) 1 [arXiv:astro-ph/0302207].

APPENDIX A: RELATIVISTIC TRANSFORMATIONS

For the energy and time transformation between rest-frame to observer-frame, which includes not only the common relativistic transformation but also the cosmological expansion, we use

$$E' = \frac{(1+z)}{\delta} E_{obs} , \quad (A1)$$

$$\Delta t' = \frac{\delta}{(1+z)} \Delta t_{obs} , \quad (A2)$$

where δ is the relativistic Doppler factor, also known as bulk Lorentz factor and z the AGN redshift ⁶.

There are luminosity transformations [17] which consider the observed integrated spectrum and solid angle distributions for moving, isotropic sources and for a continuous standard conical jets. However, in order to proceed in a more general way (i.e. model independent) we consider the following jet photon luminosity transformation

$$L'_j = \left(\frac{1+z}{\delta} \right)^2 L_{jobs} . \quad (A3)$$

APPENDIX B: OUTFLOW ANGLE, DOPPLER FACTORS AND DISTRIBUTIONS

In order to obtain a more accurate number in the exponent, γ , in the power law formula ($\delta^{-\gamma}$) for each Doppler Factor estimation model distribution, we enlarge our 39 data of the Doppler factor estimation model (there is one for each source) calculating the Doppler factor for each knot in the source. The method for calculating these Doppler factors is described in the following lines.

First, we calculate the apparent transverse velocity $\beta_{app}(j, k)$ corresponding to each knot (index k) for its AGN source (index j), given by ⁷

$$\beta_{app}(j, k) = \frac{\mu(j, k) d_m(j)}{c} , \quad (B1)$$

⁶ There should not be any misleading impression with the fact that the redshift means a receding object and most Doppler factors values an approaching source, because the redshift is due to cosmological effects and the Doppler factor to the moving knots in the jets.

⁷ The formula from Pearson&Zensus (1987) widely used in older papers is replaced by Eqs. (B1,B2) which consider a non-zero cosmological constant.

where $\mu(j, k)$ is the proper motion for each knot in the source, $d_m(j)$ is the “proper motion distance” to the source, calculated using [39]

$$d_m(j) = \frac{c}{H_0} \int_0^{Z(j)} \sqrt{(1+z)^2(1+\Omega_m z) - z(2+z)\Omega_\Lambda} dz , \quad (\text{B2})$$

with the Hubble constant $H_0 = 71 \text{ Km s}^{-1} \text{ Mpc}^{-1}$, the matter density $\Omega_m = 0.27 \pm 0.04$, and dark energy density $\Omega_\Lambda = 0.73 \pm 0.04$, according to WMAP latest results [40].

Then, we calculate the angle to the line of sight, $\theta(j, k)_{mod}$, for each proper motion component and its corresponding Doppler factor for each estimation model (the index $mod = \text{EQ, IC, Var}$), using

$$\theta(j, k)_{mod} = \arctan \left[\frac{2\beta_{app}(j, k)}{\beta_{app}(j, k)^2 + \delta(j)_{mod}^2 - 1} \right] . \quad (\text{B3})$$

In the case of Minimum Doppler factor, which gives the minimum angle, we use

$$\theta(j, k)_{min} = \text{arccot} [\beta_{app}(j, k)] . \quad (\text{B4})$$

From the distribution of $\theta(j, k)_{mod}$ for each source, we obtain its mean value $\langle \theta \rangle_{(j)mod}$ and assign it to the source, which is well justified [24]. Thus, we can construct the Doppler factor distribution for each model in terms of the Doppler factor of the knots for each AGN source.

$$\delta(j, k)_{mod} = \frac{\sqrt{1 - \beta(j, k)_{mod}^2}}{1 - \beta(j, k)_{mod} \cos \langle \theta \rangle_{(j)mod}} , \quad (\text{B5})$$

where

$$\beta(j, k)_{mod} = \frac{\beta_{app}(j, k)}{\beta_{app}(j, k) \cos \langle \theta \rangle_{(j)mod} + \sin \langle \theta \rangle_{(j)mod}} . \quad (\text{B6})$$

We discard Doppler factors that could correspond to jets affected by significant bends, twists and inward moving features.

APPENDIX C: THE AGN SAMPLE: MODEL PARAMETERS

TABLE I: BL Lacs

Source	Alias	Redshift	Lum. ($W Hz^{-1}$)	Comp.	μ_r ($mas yr^{-1}$)	δ_{EQ}	δ_{IC}	δ_{Var}	Ref.
(1)	(2)	(3)	(4)	(5)	(6)	(7)	(8)	(9)	(10)
0235+164	OD 160	0.94	1.2×10^{27}	. . .	2.35	3.7	5	16.32	G93
				B1	0.93				J01
				B2	0.61				J01
0735+178	OI 158	0.424	2.6×10^{26}	NE	0.18	6.6	5.6	3.17	C88
				. . .	0.64				G93
				K1/U1	0.14				H00
				B	0.17				K04
				C	0.64				K04
				D	-0.18				K04
				C0	0.44				V94
0754+100		0.266	1.3×10^{27}	B	0.70	0.48	0.85	5.52	K04
				C	0.05				K04
0851+202	OJ 287	0.306	2.4×10^{26}	SW1-2	0.28	12	6.8	18.03	C88
				. . .	0.37				G93
				. . .	0.23				G97
				K3/U3	1.01				H00
				B3	0.43				J01
				B2	0.54				J01
				B1+D1+F1	0.67				J01
				C	0.52				K04
				D	0.37				K04
				E	0.31				K04
				K1	0.20				V94
				K2	0.27				V94
1219+285	W Comae	0.102	1.1×10^{25}	B9	0.13	0.14	0.15	1.56	J01
				B3+B8	0.32				J01
				B7	0.60				J01
				B2+B6	0.47				J01
				B1+B5	0.50				J01
				B	0.08				K04
				C	0.02				K04
				D	0.48				K04
1749+096	4C 73.18	0.32	1.3×10^{27}	K3/U3	0.06	18	11	15.85	H00
				K2/U2	0.22				H00
				K1/U1	0.25				H00
				B	0.06				K04
				C	0.15				K04
1803+784		0.68	1.8×10^{27}	. . .	0.25	5.6	6.6	6.45	G93
				. . .	0.00				G97
				B	-0.01				K04
				. . .	0.00				V94
1807+698	3C 371	0.05	7.3×10^{24}	. . .	6.18	0.44	0.54	1.8	G93
				B	0.01				K04
				C	0.12				K04
				D	0.85				K04
				E	0.26				K04
2007+777		0.342	2.7×10^{26}	. . .	0.25	2.9	3.6	5.13	G93
				. . .	0.18				G97
				U3	0.04				H00
				U2	0.02				H00
				U1	0.20				H00
				D	-0.04				K04

TABLE I: – Continued

Source	Alias	Redshift	Lum. ($\text{W } Hz^{-1}$)	Comp.	μ_r ($\text{mas } yr^{-1}$)	δ_{EQ}	δ_{IC}	δ_{Var}	Ref.
(1)	(2)	(3)	(4)	(5)	(6)	(7)	(8)	(9)	(10)
2200+420	BL Lac	0.069	3.7×10^{25}	C2	0.18	5.2	3.4	3.91	V94
				1-4	0.76				C88
				. . .	1.62				G93
				. . .	0.99				G97
				S10	1.15				J01
				S9	1.91				J01
				S8	0.71				J01
				S7	1.36				J01
				B	1.41				K04
				C	1.12				K04
				D	0.99				K04
				E	1.09				K04
				S1	1.20				V94
				S2	1.10				V94
				S3	1.10				V94
				S5	1.00				V94

TABLE II: Quasars

Source	Alias	Redshift	Lum. ($\text{W } Hz^{-1}$)	Comp.	μ_r ($\text{mas } yr^{-1}$)	δ_{EQ}	δ_{IC}	δ_{Var}	Ref.
(1)	(2)	(3)	(4)	(5)	(6)	(7)	(8)	(9)	(10)
0016+731		1.781	3.2×10^{27}	. . .	0.31	5.7	7.9	18.37	G93
				. . .	0.30				G97
				B	0.07				K04
				. . .	0.22				V94
0106+013	4C 01.02	2.107	7.9×10^{27}	. . .	0.28	14	15	8.62	G93
				B	0.28				K04
				C	0.27				K04
				C2	0.20				V94
0133+476	DA 55	0.859	3×10^{27}	B	0.04	12	13	7.09	K04
0212+735		2.367	1.9×10^{28}	. . .	0.09	5.6	7.1	4.16	C88
				. . .	0.13				G93
				. . .	0.13				G97
				B	0.08				K04
				C	-0.01				K04
				C2	0.09				V94
				C3	0.07				V94
				C4	-0.14				V94
				. . .	0.36				G97
				B	0.23				K04
				. . .	0.30				V94
0333+321	NRAO 140	1.263	3.2×10^{27}	B	0.15	29	13	6.48	C88
				. . .	0.21				G93
				. . .	0.18				G97
				B	0.18				K04
				C	0.20				K04
				D	0.40				K04
				E	-0.08				K04

TABLE II: – Continued

Source	Alias	Redshift	Lum. (W $H z^{-1}$)	Comp.	μ_r (mas yr^{-1})	δ_{EQ}	δ_{IC}	δ_{Var}	Ref.
(1)	(2)	(3)	(4)	(5)	(6)	(7)	(8)	(9)	(10)
0336-019	CTA 26	0.852	3×10^{27}	B	0.15	13	12	19.01	V94
				C4	0.18				J01
				C3	0.42				J01
				B	0.22				K04
0420-014	OA 129	0.915	6.3×10^{27}	C	0.21	21	13	11.72	K04
				B	0.20				J01
				B	0.03				K04
				C	0.29				K04
0528+134	PKS 0528+134	2.07	4.6×10^{28}	K2/U2	0.16	0.71	2	14.22	H00
				F2	0.40				J01
				B1+F3	0.26				J01
				B2+F4	0.33				J01
				B3	0.19				J01
				B4	0.15				J01
				B	0.08				K04
0552+398	DA 193	2.365	3.6×10^{28}	. . .	0.06	1.2	2.2	14.2	G93
				. . .	0.06				G97
				. . .	0.04				V94
				B	0.13				K04
0804+499	4C 71.07	1.432	1.9×10^{27}	. . .	0.35	8.5	6.7	10.67	K04
0836+710		2.17	1.39×10^{28}	. . .	0.27				G93
. . .		0.27	G97						
B		0.24	J01						
B		0.23	V94						
D		0.14	V94						
0923+392		4C 39.28	0.698	1×10^{28}	A-C				0.01
	B				0.16	C88			
	. . .				0.22	G93			
	. . .				0.19	G97			
	B				0.07	K04			
	C				0.01	K04			
	B				0.18	V94			
1156+295	4C 29.45	0.729	1×10^{27}	D	0.02	2.2	4.9	9.42	V94
				. . .	1.58				G93
				. . .	1.24				G97
				B2	0.34				J01
				B3	0.54				J01
				B	0.22				K04
				. . .	1.15				V94
1226+023	3C 273	0.158	1.5×10^{27}	C3	0.79	8.3	4.6	5.71	C88
				C4	0.99				C88
				C5	1.20				C88
				C7a	0.76				C88
				. . .	1.62				G93
				. . .	0.88				G97
				K10/U10	0.77				H00
				K9/U9	0.94				H00
				K8/U8	1.15				H00
				K7/U7	1.06				H00
				K4/U4	0.99				H00
				B5+E2	0.33				J01
				B4+E1	0.85				J01
				B3	0.66				J01
				B2	0.61				J01
				B1+G1	0.68				J01
				H5+K6+D1	1.60				J01

TABLE II: – Continued

Source	Alias	Redshift	Lum. (W $H z^{-1}$)	Comp.	μ_r (mas yr^{-1})	δ_{EQ}	δ_{IC}	δ_{Var}	Ref.
(1)	(2)	(3)	(4)	(5)	(6)	(7)	(8)	(9)	(10)
				H3+K5+D2	0.70				J01
				B	1.05				K04
				C	1.36				K04
				D	0.83				K04
				E	1.27				K04
				F	0.79				K04
				G	0.41				K04
				I	0.88				K04
				C2	1.15				V94
				C3	0.79				V94
				C4	0.99				V94
				C5	1.20				V94
				C7	0.65				V94
				C7a	0.76				V94
				C8	0.92				V94
				C9	0.82				V94
1253-055	3C 279	0.538	1.3×10^{28}	. . .	0.50	14	14	16.77	C88
				B2	0.11				C88
				. . .	0.68				G93
				. . .	0.14				G97
				K4/U4	0.17				H00
				K1/U1	0.25				H00
				B3	0.18				J01
				B2	0.17				J01
				E2+B1	0.27				J01
				D	0.31				J01
				B	0.28				K04
				C3	0.12				V94
				. . .	0.50				V94
1308+326	OR 017	0.997	5.8×10^{27}	K2/U2	0.19	4.3	5.2	11.38	H00
				K1/U1	0.96				H00
				. . .	0.45				G97
				K1	0.13				V94
				K2	0.75				V94
				K3	0.29				V94
				B	0.31				K04
1510-089	4C 09.56	0.36	3.4×10^{26}	K3/U3	0.45	10	11	13.18	H00
				B1	0.51				J01
				D1	0.28				J01
				D2	0.63				J01
				B	0.85				K04
				C	0.57				K04
1633+382	4C 38.41	1.807	6.5×10^{27}	B3	0.14	0.83	2.2	8.83	J01
				B1	0.20				J01
				B	0.15				K04
				C	0.10				K04
1641+399	3C 345	0.594	5.9×10^{27}	C2	0.48	1.5	4.1	7.45	C88
				C3	0.30				C88
				C4	0.30				C88
				. . .	0.66				G93
				. . .	0.33				G97
				B	0.49				K04
				C	0.37				K04
				C2	0.47				V94
				C3	0.30				V94

TABLE II: – Continued

Source	Alias	Redshift	Lum. (W $H z^{-1}$)	Comp.	μ_r (mas yr^{-1})	δ_{EQ}	δ_{IC}	δ_{Var}	Ref.
(1)	(2)	(3)	(4)	(5)	(6)	(7)	(8)	(9)	(10)
1928+738	4C 73.18	0.303	6.2×10^{26}	C4	0.31	3.4	3.4	3.71	V94
				C5	0.23				V94
				A1-4	0.60				C88
				. . .	0.81				G93
				. . .	0.39				G97
				B	0.29				K04
				C	0.30				K04
				E	0.12				K04
				A1	0.32				V94
				B	0.37				V94
				C	0.34				V94
				C2	0.51				V94
				C3	0.57				V94
				C4	0.40				V94
				C6	0.40				V94
2021+614	OW 637	0.227	2.6×10^{26}	C7	0.60	0.9	1.1	1.59	V94
				C9	0.31				V94
				. . .	0.04				C88
				. . .	0.05				G93
				. . .	0.02				G97
				B	0.04				K04
				C	0.05				K04
				. . .	0.02				V94
				. . .	0.01				C88
				. . .	0.01				G93
2134+004	PHL 61	1.932	2.9×10^{28}	B	0.02	15	27	11.49	K04
				. . .	0.01				C88
				. . .	0.01				G93
				B	0.02				K04
2145+067	4C 06.69	0.999	1.1×10^{28}	B	-0.01	15	21	7.81	K04
				C	0.03				K04
				D	0.03				K04
2223-052	3C 446	1.404	1.2×10^{28}	. . .	0.14	18	16	11.39	G93
				B	0.49				K04
				C	0.31				K04
2230+114	CTA 102	1.037	4.3×10^{27}	. . .	0.65	1	1.5	14.23	C88
				. . .	0.69				G93
				B3	0.25				J01
				B2	0.34				J01
				B1	0.33				J01
				B	0.03				K04
				C	-0.05				K04
				E	-0.23				K04
				2	0.05				C88
				4	0.35				C88
2251+158	3C 454.3	0.859	1.2×10^{28}	. . .	0.48	5.6	4.6	21.84	G93
				. . .	0.09				G97
				B3	0.14				J01
				B2	0.34				J01
				B1	0.53				J01
				B	0.04				K04
				2	0.05				V94
				3	-0.05				V94
				4	0.35				V94
				5	0.21				V94

TABLE III: Radio Galaxy & Seyfert

Source	Alias	Redshift	Lum. (W $H z^{-1}$)	Comp.	μ_r (mas yr^{-1})	δ_{EQ}	δ_{IC}	δ_{Var}	Ref.
(1)	(2)	(3)	(4)	(5)	(6)	(7)	(8)	(9)	(10)
1845+797	3C 390.3	0.057	2.9×10^{24}	. . .	0.98	0.37	0.38	1.16	G93
				B	0.54				K04
				C	0.60				K04
0430+052	3C 120	0.033	8.2×10^{24}	A	1.35	11	4.1	0.98	C88
				B	2.53				C88
				C	2.47				C88
				D	2.66				C88
				E	2.54				C88
				. . .	3.55				G93
				. . .	2.06				G97
				K1B/U1B	1.62				H00
				K1A/U1A	2.22				H00
				B	1.77				K04
				C	1.80				K04
				D	1.36				K04
				G	1.59				K04
				I	1.51				K04
				H	2.08				K04
				A	1.35				V94
				B	2.53				V94
				C	2.47				V94
				D	2.66				V94
				E	2.54				V94

Note.- The acronyms used in the references for the proper motion, given in column (10), correspond to: C88 ([27]), G93 ([19]), G97 ([10]), H00 ([25]), J01 ([26]), K04 ([20]), and V94 ([28]).

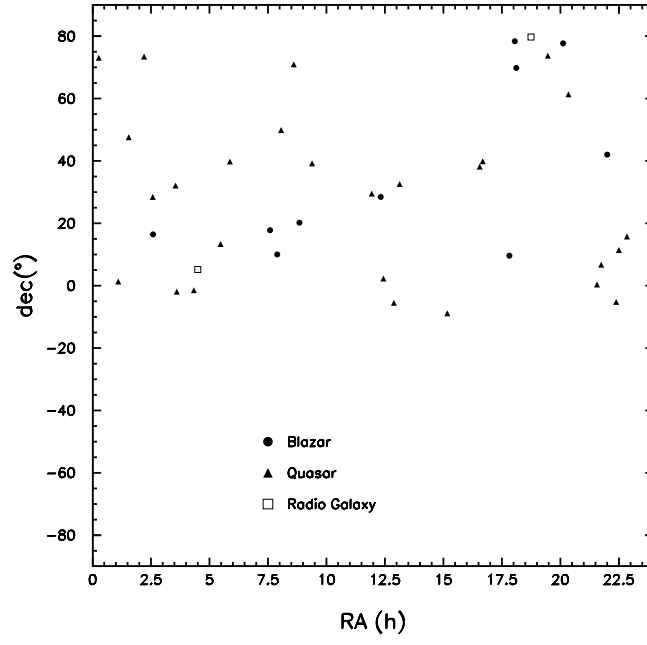


FIG. 1: Distribution of the AGNs sample given in right ascension and declination angles.

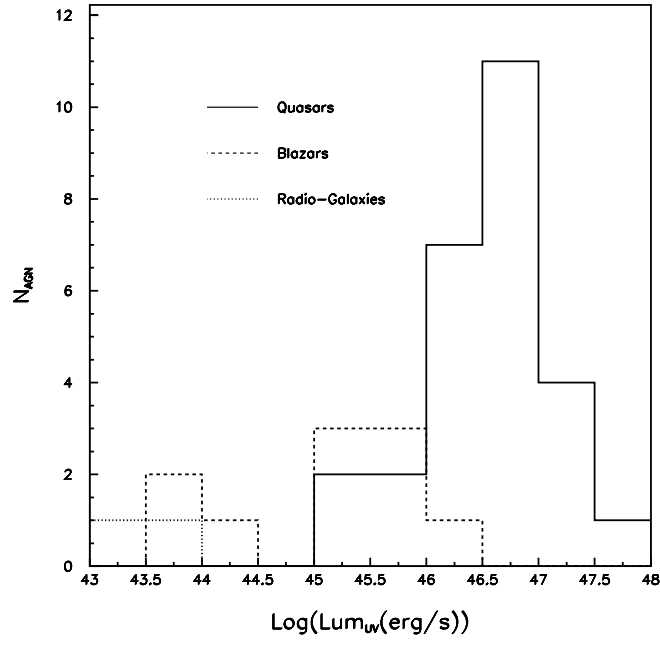


FIG. 2: Distribution of the observed UV-Luminosity in the sample.

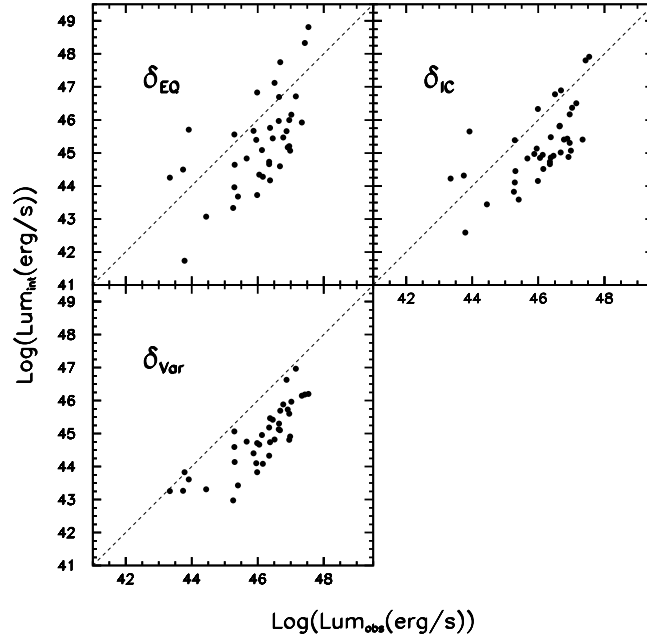


FIG. 3: Intrinsic versus observed luminosities according to the Doppler estimation model.

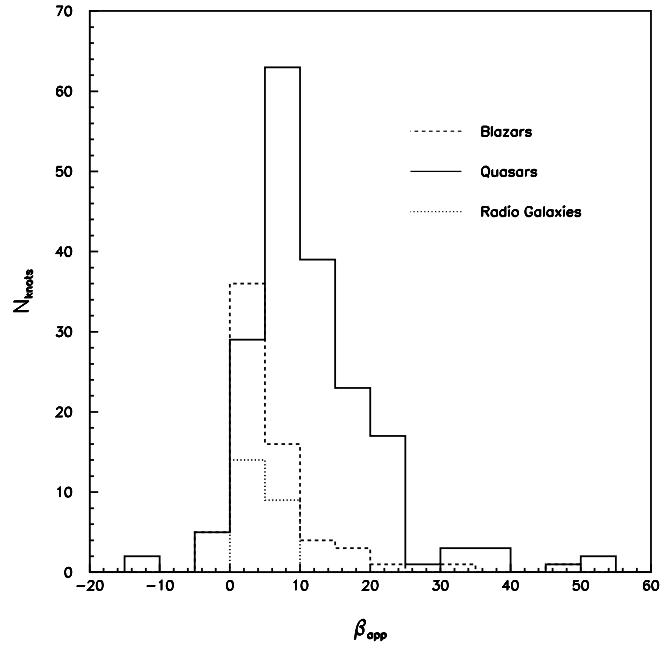


FIG. 4: Apparent transverse velocity distribution in the sample.

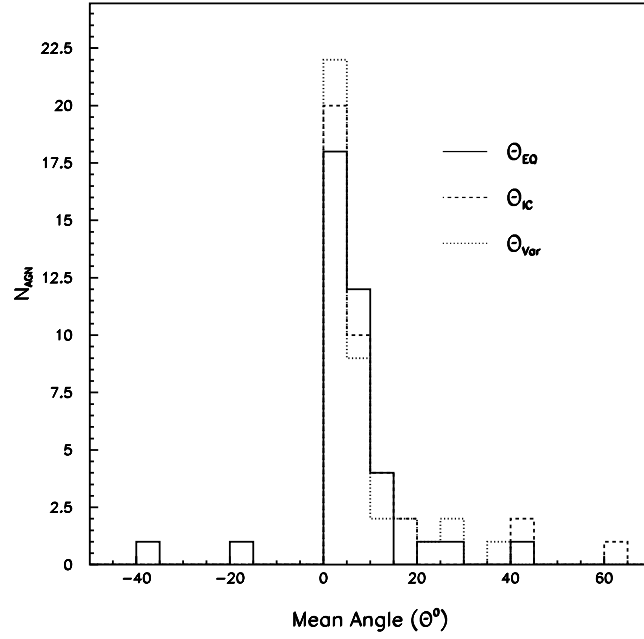


FIG. 5: Distribution of the mean angle to the line of sight in the sample.

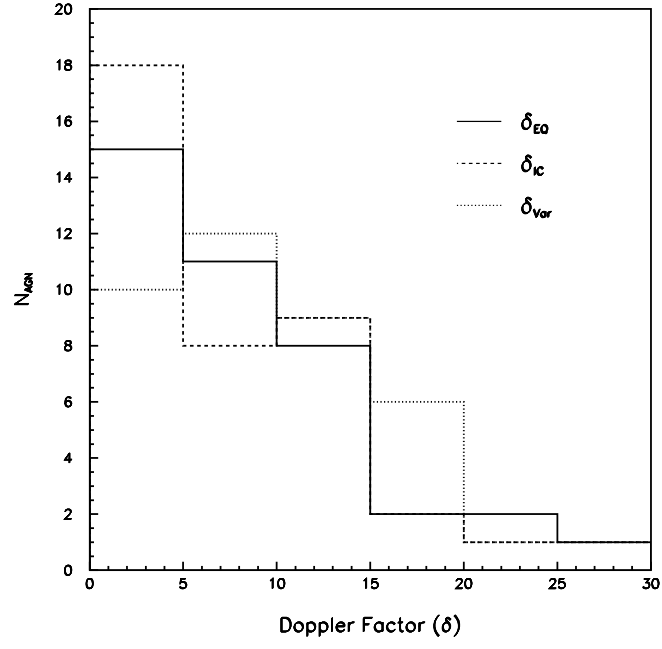


FIG. 6: Doppler factor model distribution in the sample.

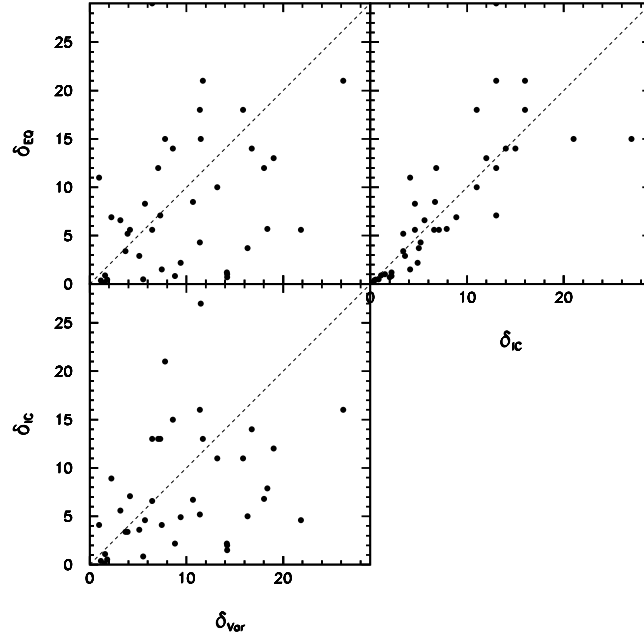


FIG. 7: Comparison of the different types of Doppler factors for the sample.

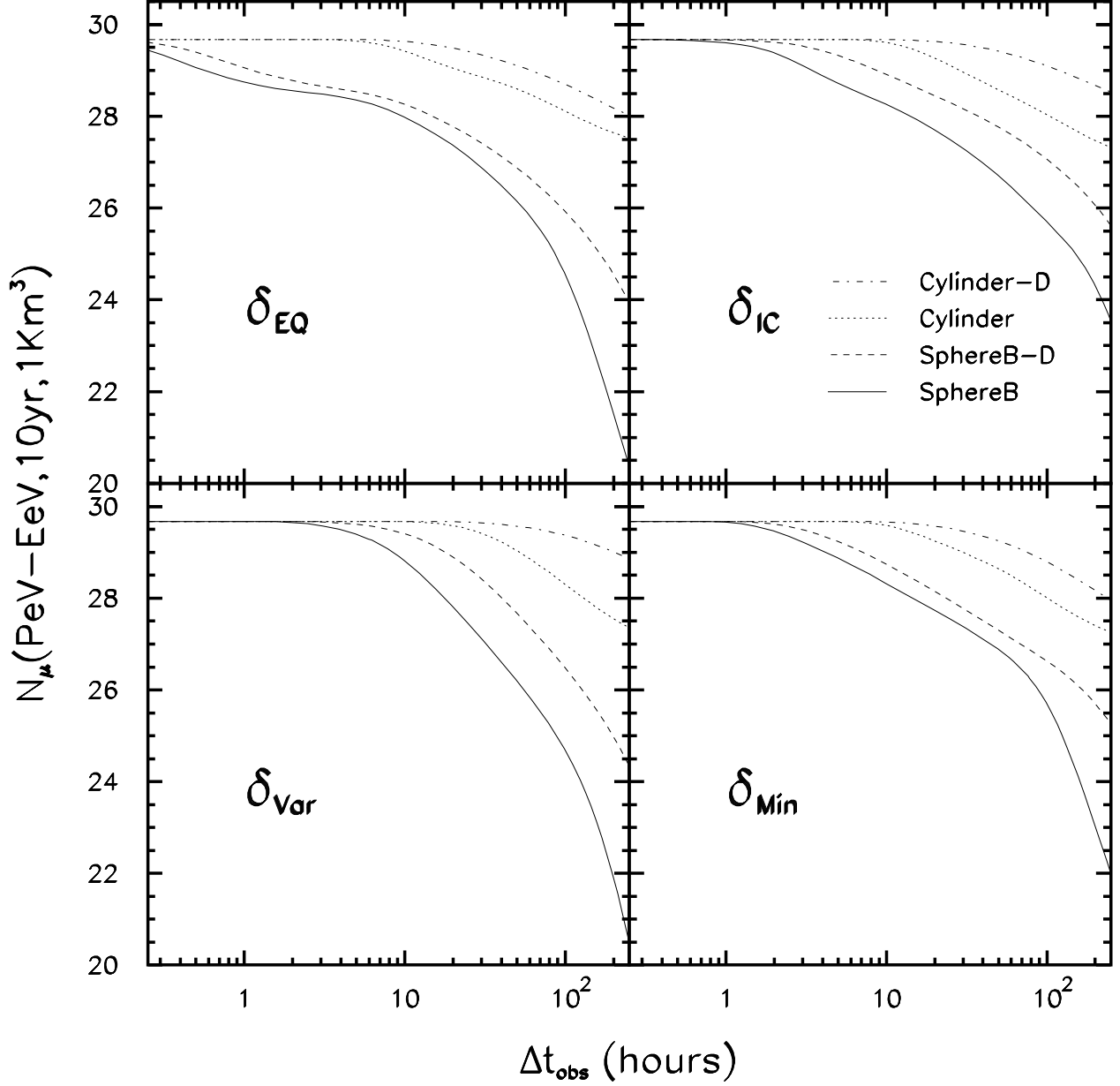


FIG. 8: Expected total AGN ν_μ -induced events as a function of the variability time, for different assumptions in the model parameters studied. The maximum flux is normalized with the Waxman-Bahcall limit [14] and $p = 2$ is taken in the energy spectrum. “D” stands for the use of δ distribution.

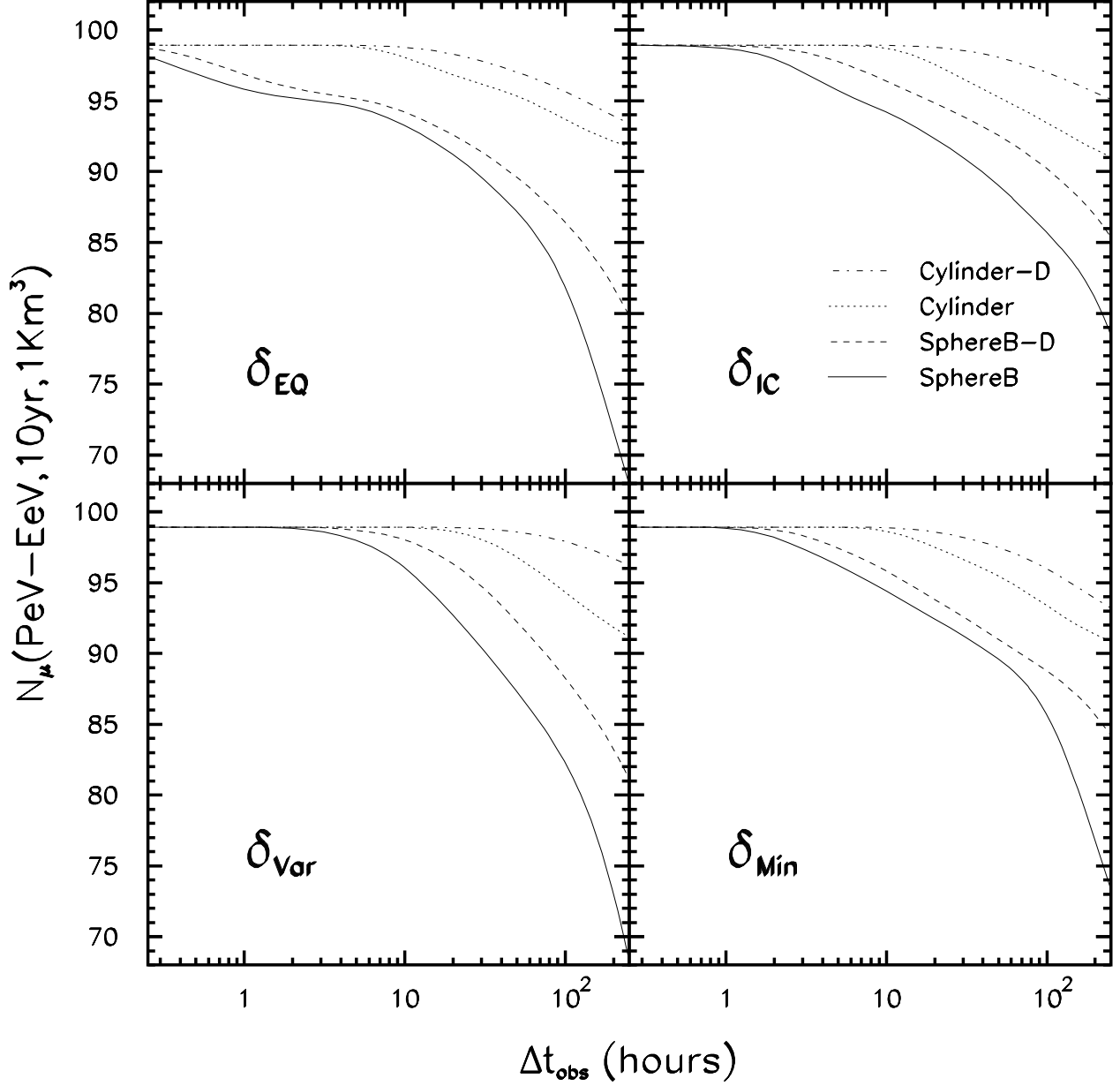


FIG. 9: Expected total AGN ν_μ -induced events as a function of the variability time, for different assumptions in the model parameters studied. The maximum flux is normalized with the benchmark used by the IceCube Collab. [15] and $p = 2$ is taken in the energy spectrum. “D” stands for the use of δ distribution.

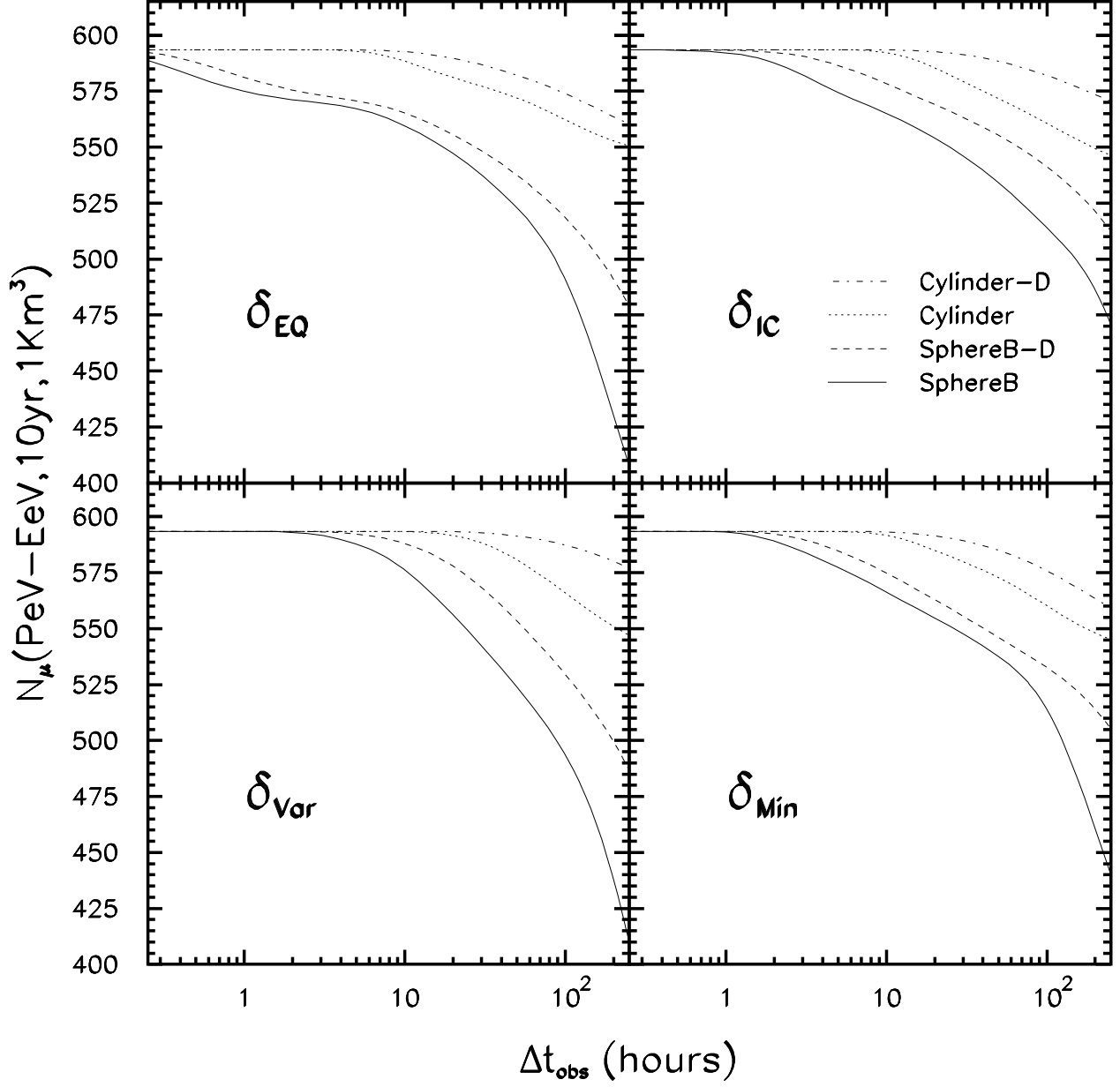


FIG. 10: Expected total AGN ν_μ -induced events as a function of the variability time, for different assumptions in the model parameters studied. The maximum flux is normalized with the γ -ray bound [16] and $p = 2$ is taken in the energy spectrum. “D” stands for the use of δ distribution.

ν flux limit	Without δ distribution				Using δ distribution			
	δ_{EQ}	δ_{IC}	δ_{Var}	δ_{Min}	δ_{EQ}	δ_{IC}	δ_{Var}	δ_{Min}
<i>WB</i>	1.53	0.75	1.45	1.08	0.81	0.56	0.89	0.53
<i>IceCube</i>	2.79	1.36	2.64	1.97	1.48	1.02	1.62	0.96
γ -ray	6.84	3.34	6.47	4.82	3.62	2.51	3.98	2.35

TABLE IV: Separation in terms of N_σ between the number of events obtained for the spherical and cylindrical geometries, using the three ν flux limits, all δ cases and $\Delta t_{obs} = 10$ days.

ν flux limit	Without δ distribution					
	EQ-IC	EQ-Var	EQ-Min	IC-Var	IC-Min	Var-Min
<i>WB</i>	0.68	0.04	0.35	0.59	0.31	0.31
<i>IceCube</i>	1.25	0.08	0.64	1.09	0.56	0.56
γ -ray	3.05	0.18	1.57	2.67	1.38	1.38
	Using δ distribution					
	EQ-IC	EQ-Var	EQ-Min	IC-Var	IC-Min	Var-Min
<i>WB</i>	0.33	0.08	0.26	0.24	0.07	0.18
<i>IceCube</i>	0.61	0.15	0.48	0.44	0.13	0.32
γ -ray	1.49	0.36	1.17	1.09	0.32	0.79

TABLE V: Separation in terms of N_σ between the number of events obtained for different pairs of δ cases and the three ν flux limits, using the spherical geometry and $\Delta t_{obs} = 10$ days.

ν flux limit	Without δ distribution					
	EQ-IC	EQ-Var	EQ-Min	IC-Var	IC-Min	Var-Min
<i>WB</i>	0.04	0.03	0.05	0.01	0.01	0.02
<i>IceCube</i>	0.07	0.05	0.09	0.02	0.02	0.04
γ -ray	0.18	0.13	0.23	0.04	0.05	0.09
	Using δ distribution					
	EQ-IC	EQ-Var	EQ-Min	IC-Var	IC-Min	Var-Min
<i>WB</i>	0.09	0.16	0.01	0.06	0.10	0.16
<i>IceCube</i>	0.17	0.29	0.02	0.11	0.19	0.30
γ -ray	0.43	0.70	0.04	0.27	0.47	0.73

TABLE VI: Separation in terms of N_σ between the number of events obtained for different pairs of δ cases and the three ν flux limits, using the cylindrical geometry and $\Delta t_{obs} = 10$ days.

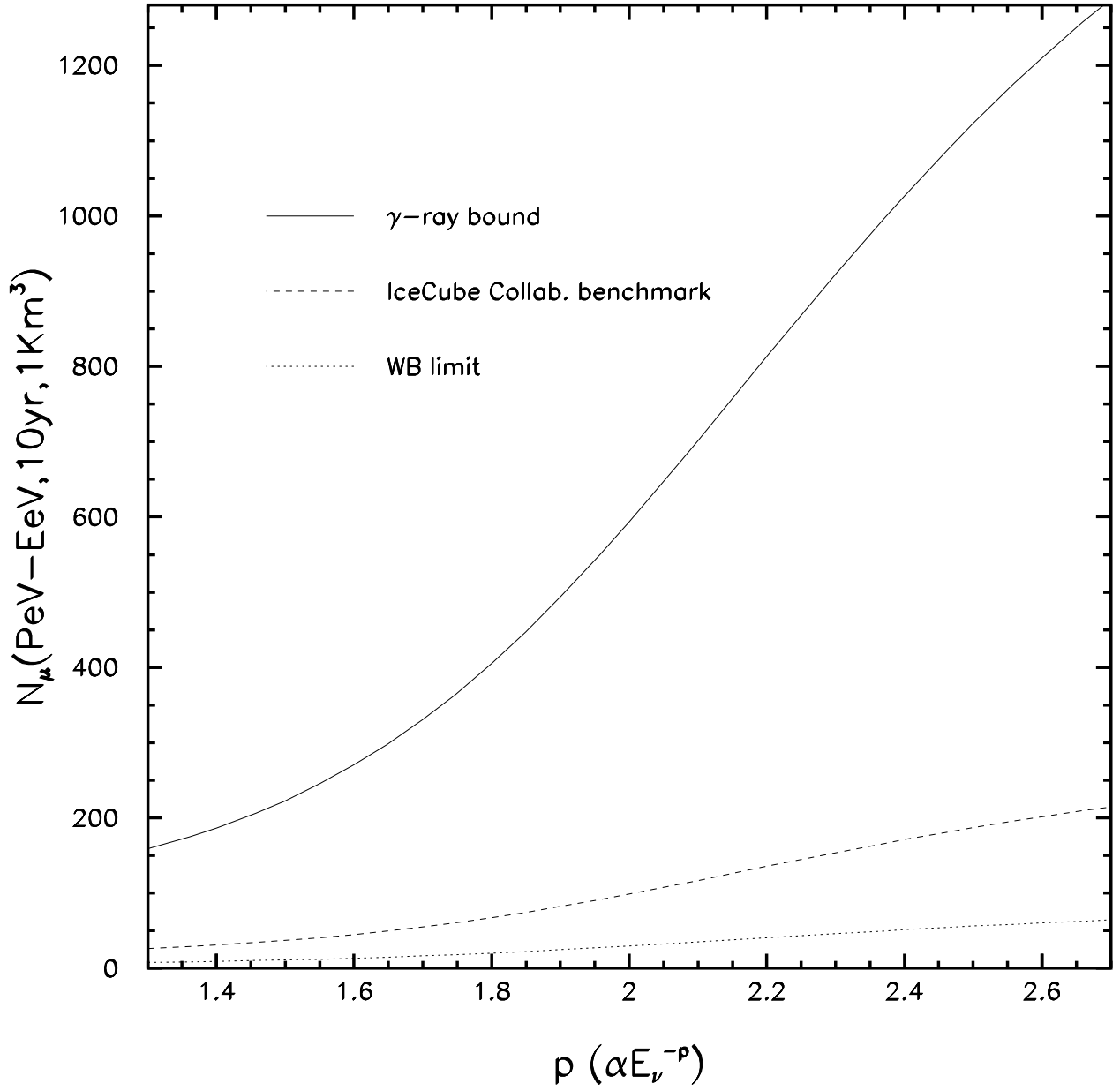


FIG. 11: Expected total AGN muon neutrino induced events normalized with different bounds of the ν flux limit as a function of the exponent in the power law assumed in the AGN- ν_μ flux.